



HAL
open science

Halogen Bearing Amphiboles, Aqueous Fluids, and Melts in Subduction Zones: Insights on Halogen Cycle From Electrical Conductivity

Geeth Manthilake, Kenneth T. Koga, Y. Peng, M. Mookherjee

► **To cite this version:**

Geeth Manthilake, Kenneth T. Koga, Y. Peng, M. Mookherjee. Halogen Bearing Amphiboles, Aqueous Fluids, and Melts in Subduction Zones: Insights on Halogen Cycle From Electrical Conductivity. *Journal of Geophysical Research: Solid Earth*, 2021, 126 (3), 10.1029/2020JB021339 . hal-03181956

HAL Id: hal-03181956

<https://uca.hal.science/hal-03181956>

Submitted on 26 Mar 2021

HAL is a multi-disciplinary open access archive for the deposit and dissemination of scientific research documents, whether they are published or not. The documents may come from teaching and research institutions in France or abroad, or from public or private research centers.

L'archive ouverte pluridisciplinaire **HAL**, est destinée au dépôt et à la diffusion de documents scientifiques de niveau recherche, publiés ou non, émanant des établissements d'enseignement et de recherche français ou étrangers, des laboratoires publics ou privés.

1 **Halogen bearing amphiboles, aqueous fluids, and melts in subduction zones:**
2 **Insights on halogen cycle from electrical conductivity**

3 G. Manthilake^{1*}, K. T. Koga¹, Y. Peng², M. Mookherjee²

4
5 ¹ Laboratoire Magmas et Volcans CNRS, IRD, OPGC, Université Clermont Auvergne, 63000
6 Clermont-Ferrand, France

7 ² Earth Materials Laboratory, Department of Earth, Ocean and Atmospheric Sciences, Florida
8 State University, Tallahassee, FL, 32306, USA

9
10
11 *Corresponding author (geeth.manthilake@uca.fr)

12
13
14 **Key Points:**

- 15 • The presence of F and Cl increases the electrical conductivity in aqueous fluids
- 16 • During dehydration, a fraction of F and Cl partitioned into solid phases
- 17 • F and Cl can be transported to the deep mantle by secondary minerals

23 **Abstract**

24 Amphiboles are hydrous minerals that are formed in the oceanic crust via hydrothermal
25 alteration. The partial substitution of halogens for OH⁻ makes amphibole one of the principal
26 hosts of Cl and F in the subducting slab. In this study, we investigated the electrical conductivity
27 of a suite of halogen bearing amphibole minerals at 1.5 GPa up to 1400 K. The discontinuous
28 electrical behavior indicate dehydration of amphibole at ~915 K. This is followed by
29 dehydration induced hydrous melting at temperatures above 1070 K. We find that the released
30 aqueous fluids have an electrical conductivity of ~0.1 S/m. This high electrical conductivity is
31 likely to explain anomalously high electrical conductivity observed in certain subduction zone
32 settings. This high electrical conductivity of an order of magnitude greater than the electrical
33 conductivity of pure aqueous fluids at similar conditions is likely due to the partitioning of the
34 F and Cl into the aqueous fluids. We also noted that subsequent to the dehydration, secondary
35 phases form due to the breakdown of the primary halogen bearing amphibole. Chemical
36 analyses of these secondary phases indicate that they are repositories of F and Cl. Hence, we
37 infer that upon dehydration of the primary halogen bearing amphibole, first the F and Cl are
38 partitioned into the aqueous fluids and then the halogens are partitioned back to the secondary
39 mineral phases. These secondary minerals are likely to transport the halogen to the deep Earth
40 and may in part explain the halogen concentration observed in ocean island basalt.

41

42

43

44

45

46 **Plain language summary**

47 Amphiboles are one of the principal mineral phases that accommodate halogens in the
48 subducting slab. The aqueous fluid released during the dehydration of amphibole dissolves and
49 transfers halogens into the overlying wedge mantle. The resulting fluid exhibits high electrical
50 conductivity. Our study also indicates that a significant portion of F and small quantities of Cl
51 carried by amphibole are partitioned back to the secondary mineral phases that result from the
52 breakdown of the primary amphibole. These secondary mineral phases are likely to transport
53 halogen into the Earth's interior and may explain the distinct halogen contents observed
54 between lower mantle-derived ocean island basalts compared to MORB sources.

55

56

57 **1. Introduction**

58 Amphiboles are hydrous minerals present in the altered oceanic crust and play a vital
59 role in transporting hydrophile elements including halogen into the deep mantle via subduction
60 of oceanic plates (Debret et al., 2016; Ito et al., 1983). The crystal structure of amphibole
61 consists of corner-sharing tetrahedral units linked to form double chains and edge-sharing
62 octahedral units. The octahedral strip is sandwiched between two tetrahedral double chains with
63 their apices pointing towards each other forming an I-beam. These minerals also contain ~ 2 wt
64 % water crystallographically bound as hydroxyl (OH⁻) units. The interaction of saline seawater
65 with oceanic crust often helps to incorporate Cl and F into the amphibole crystal structure.
66 These halogen ions, Cl⁻ and F⁻ readily substitutes for the hydroxyl (OH⁻) units (Kendrick et al.,
67 2011). As the subducting slabs experience higher temperatures at depths, hydrous minerals
68 including amphibole dehydrate. And upon dehydration, Cl and F in the amphibole crystal
69 structure are likely to partition into the released aqueous fluid. However, based on experimental
70 results it seems that Cl is likely to partition into aqueous fluid far more easily than F (Bernini

71 et al., 2013; Fabbri et al., 2013a; Fabbri et al., 2013b). When amphibole or apatite is
72 present with an aqueous fluid, F partitions into these minerals instead of fluid (Brenan, 1993;
73 Wu & Koga, 2013, 2018). During partial melting, these elements are incompatible with
74 minerals (Beyer et al., 2012, 2016; Dalou et al., 2012, 2014). However, highly incompatible Cl
75 may readily partition into the melt phase while moderately incompatible F may incorporate into
76 minerals with hydroxyl-sites (Van den Bleeken & Koga, 2015; Mathez & Webster, 2005;
77 Webster et al., 2009).

78 Magnetotelluric (MT) studies provide crucial information on the presence of aqueous
79 fluids and/or melts in Earth's interior. Interpretation of MT results based on the laboratory-based
80 electrical conductivity of minerals, fluids, and melts has been fundamental in the
81 characterization of the degree of mantle hydration (Freitas & Manthilake, 2019; Soyer &
82 Unsworth, 2006), circulation of aqueous fluids in the upper mantle (Manthilake et al., 2015;
83 Manthilake et al., 2016), and melting (McGary et al., 2014; Zhang et al., 2014). A few studies
84 have discussed the electrical conductivity of fluids bearing systems (Guo & Keppler, 2019; Guo
85 et al., 2015; Reynard et al., 2011; Sakuma & Ichiki, 2016; Shimojuku et al., 2012, 2014; Sinmyo
86 & Keppler, 2017). These studies have characterized saline fluid compositions that are
87 appropriate for shallow crustal fluids. However, the fluids released in subduction zones and at
88 conditions relevant for deeper mantle are likely to be different from such crustal fluids. At
89 greater depths, aqueous fluids often evolve to supercritical fluids and may have enhanced
90 electrical conductivities (Manthilake et al., 2015; Mitchell & Nellis, 1982). In addition, the
91 effect of halogen on aqueous fluids under these conditions remains unknown.

92 The thermodynamic stability of amphibole in subducting slabs is often dictated by the
93 composition. For instance, the hydrous amphibole phase is likely to break down at around ~80
94 km depth (Schmidt & Poli, 1998). In contrast, the thermal stability of F⁻ and/or Cl⁻ bearing
95 amphibole is greater and may be stable beyond depths of 80 km (Foley, 1991; Holloway &

96 Ford, 1975). A related key question is, when halogen bearing amphiboles dehydrate, do all the
97 halogens partition to the aqueous fluids and eventually recycled back to the Earth's surface? Or
98 is there a fraction of halogens sequestered into nominally anhydrous phases and are transported
99 into the deep Earth?

100 The relatively stable halogen levels in world oceans suggest that the amount of halogen
101 entering into the Earth's interior via subduction would go through efficient recycling processes
102 and re-emitted at the arc volcanoes (Wallace, 2005). While most of the halogens are recycled
103 at shallower depths (Scambelluri et al., 2004), the recent reports of higher concentrations of Cl
104 and F in the lower mantle-derived oceanic island basalts magmas (OIB) indicate a possibility
105 of subducting halogens into the Earth's lower mantle (Hanyu et al., 2019; Jackson et al., 2015;
106 Kovalenko et al., 2006; Rose-Koga et al., 2017). These recent reports have also prompted
107 experimental studies on the solubility of halogen in mineral phases of the transition zone and
108 lower mantle (Roberge et al., 2017; Yoshino & Jaseem, 2018) which also suggests that these
109 deep mantle phases could sequester halogens to the deep Earth.

110 Hence, in order to understand the fate of halogens during the dehydration of halogen
111 bearing amphibole at subduction zone conditions, in this study, we investigate the electrical
112 conductivity of four chemically distinct, Cl, and F bearing amphibole compositions at 1.5 GPa
113 up to 1400 K. We characterize the electrical conductivity of the aqueous fluid and if halogens
114 are partitioned into the fluids, does that affect the electrical conductivity and we compare
115 laboratory data with MT data to better understand subduction settings where these results are
116 applicable. Also, we characterize the secondary mineral phases to evaluate whether all the
117 halogens are lost to the aqueous fluids or are there a fraction of halogen sequestered into
118 secondary phases which may transfer it to deep Earth and explain the halogen concentrations
119 observed in OIB.

120 2. Methods

121 For the electrical conductivity experiments, four natural amphibole samples, ferri-
122 kaersutite (Dontresse, Cézalier, France), actinolite (Russel, NY, USA), hastingsite (Lenzo,
123 Italy), and tremolite (Russel, NY, USA) were used. These four distinct samples have varying
124 concentrations of halogens i.e., Cl and F. The chemical composition of amphiboles was
125 analyzed using a Cameca SxFiveTactis electron microprobe. The electron probe microanalysis
126 was conducted with an accelerating voltage of 15 kV and a beam current of 20 nA. F and
127 Cl were measured by electron microprobe using three Fe interference-free Thallium acid
128 phthalate (TAP) crystals (Rose-Koga et al., 2020). The concentrations of F and Cl in the four
129 natural amphibole samples were also determined using an IMS 1270 secondary-ion mass
130 spectrometer (SIMS) at Centre de Recherches Pétrographiques et Géochimiques (CRPG)
131 Nancy, France.

132 To prepare the samples for the electrical conductivity measurements, first, the large
133 crystals of natural amphibole were broken down to smaller sized crystals. Then, the inclusion-
134 free smaller sized crystals were handpicked under the binocular microscope. These smaller
135 inclusion-free crystals were then crushed into finely powdered samples. These powdered
136 samples were placed in cylindrical rhenium (Re) capsule and hot-pressed at 1.5 GPa and 700 K
137 for 1 hour. Hot pressing of the sample and electrical conductivity experiments at high pressures
138 and temperatures were performed using a 1500-ton multi-anvil apparatus installed at the
139 Laboratoire Magmas et Volcans. The electrical conductivity measurements were performed in
140 18/11 multi-anvil assemblies i.e., 18 mm edge length of the MgO octahedral pressure medium
141 and 11 mm of the truncated edge length of the first stage anvils made up of tungsten carbide
142 (WC) (**Fig. 1a**). Pre-sintered cylindrical samples were placed in a polycrystalline hBN capsule.
143 The high purity hBN, sintered at higher temperature and pressure without boron (B) binder
144 (BNHP- FINAL Advanced Materials, France) ensured that there were no B₂O₃ forming

145 reactions with the aqueous fluids. The fine grain size of the sintered hBN also reduced the
146 possibility of fluid escape from the sample at high temperatures. Nickel (Ni) disks were placed
147 at the opposite ends of the cylindrical sample. These Ni disks were used as electrodes for the
148 electrical conductivity measurements. These Ni disks also served to regulate the oxygen
149 fugacity (f_{O_2}) Ni-NiO which is similar to the Fayalite-Magnetite-Quartz (FMQ) buffer (Frost,
150 1991). The temperature of the sample was monitored with a W₉₅Re₅-W₇₄Re₂₆ thermocouple
151 junction placed at one side of the sample. Sample resistance was obtained using the leads from
152 the thermocouple and a separate W₉₅Re₅ cable placed at the opposite side of the sample. MgO
153 ceramic sleeves were placed to insulate the electrode wires from the furnace. To avoid the
154 exposure of assembly components to atmospheric moisture and other impurities, ceramic
155 assembly parts were baked at 1273 K and stored at 400 K in high- vacuum furnaces prior to
156 assembling.

157 Electrical resistivity was determined using the impedance spectroscopy method in the
158 frequency range of 10⁶-10¹ Hz. At the desired pressure, samples were kept at 500 K for several
159 hours to remove the absorbed moisture in the sample capsule and the surrounding area, which
160 improves the insulation resistance of the assembly (Manthilake et al., 2015). The sample
161 resistance was measured at temperature steps of 50-100 K with increasing temperature beyond
162 the thermodynamic stability of amphiboles. We have also collected data along the cooling
163 cycle. along with the heating and cooling cycle. The resistance of polycrystalline samples can
164 be modeled by a combination of resistor-capacitor (R-C) or resistor-constant phase element (R-
165 CPE) circuits (**Fig. 2**). The electrical conductivity of the polycrystalline sample can be
166 determined by the resistance from impedance spectra, and the dimension of the sample i.e.,
167 diameter and length, measured after each experiment (**Fig. 1b-e**).

168 The dependence of the electrical conductivity of the polycrystalline sample with inverse
169 temperature exhibits Arrhenius relation (**Fig.3**). The activation enthalpy (ΔH) of the conduction

170 mechanisms operating at different temperature intervals can be determined according to the
171 Arrhenius equation, $\sigma = \sigma_0 \exp(-\Delta H/RT)$, where σ is the electrical conductivity (S/m), T is
172 the absolute temperature, σ_0 is the pre-exponential factor (S/m), and R is the universal gas
173 constant (J/K.mol).

174 In addition to the chemical compositions of the natural amphiboles used for the
175 electrical conductivity studies, the chemistry and the modal abundances of the secondary
176 phases, following the *in-situ* electrical conductivity experiments, were also investigated using
177 the Cameca SxFiveTactis electron microprobe. Unreacted primary minerals and secondary
178 mineral assemblages from the breakdown of the primary amphiboles due to dehydration were
179 characterized using energy-dispersive x-ray spectroscopy (EDS) chemical mapping. The
180 composition of the fluid and the melt phases were determined by mass-balance calculations
181 based on the mineral proportions and their chemical compositions of recovered samples
182 following the dehydration and dehydration-induced partial melting (Locock, 2014).

183

184 **3. Results**

185 The discontinuous increase of electrical conductivity with increasing temperature was
186 observed in all experimental runs (**Fig. 3**). We note that heating of the sample above the pre-
187 sintering temperature does not significantly enhance the electrical conductivity. However, we
188 have observed a reduction of the noise in the impedance spectra during the high T annealing.
189 This is likely due to the healing of microcracks developed during the compression. The
190 discontinuous trends can be used to determine the changes that the sample undergoes including
191 dehydration and dehydration-induced melting (Freitas and Manthilake, 2019; Manthilake et al.,
192 2015; Manthilake et al., 2016). The electrical conductivity of amphibole was characterized by
193 two main conductivity discontinuities, the first discontinuity occur over a temperature range of
194 915-933 K and the second discontinuity is often observed over a temperature range of 1070-

195 1170 K. These observed discontinuities in electrical conductivity vs. inverse temperature can
196 be separated into three distinct temperature intervals: at temperatures lower than 900 K, the
197 electrical conductivity is dominated by the polycrystalline mineral sample, between 900 and
198 1100 K, the electrical conductivity is due to aqueous fluids released by dehydration of
199 amphibole, and at temperatures greater than 1100 K, the electrical conductivity is due to the
200 dehydration-induced hydrous silicate melt (**Fig. 3**). The dehydration temperatures observed for
201 a suite of amphiboles that are likely to be stable in different lithologies in the Earth's mantle
202 ranges between 1200 to 1300 K (Mandler & Grove, 2016). We note the enhancement in the
203 electrical conductivity is in good agreement with the dehydration-induced melting observed in
204 amphibolites (Wyllie & Wolf, 1993). The electrical conductivities of dehydrating fluids were
205 similar with little or no variations (~ 0.1 S/m) across all starting compositions. The electrical
206 conductivity of the hydrous melt produced by the melting of ferri-kaersutite, actinolite,
207 hastingsite 6, 8, and 8 S/m respectively, at the highest temperature measured in each heating
208 cycles, while tremolite exhibited slightly lower conductivity of about 2 S/m at 1403 K.

209 The increase of electrical conductivity with increasing temperature after the dehydration
210 and subsequent dehydration-induced melting of amphibole is likely to be related to (a) the
211 interconnectivity of the liquid phase governed by their ability to wet the grain boundaries, and
212 (b) the increase of fluid/melt fraction in the samples as observed in prior studies on different
213 samples (Freitas et al., 2019). It is known that the dihedral angle of aqueous fluids decreases
214 with increasing pressures and temperatures (Manthilake et al., 2015; Mibe et al., 1999; Yoshino
215 et al., 2002). This points toward the enhancement of grain boundary wetting by aqueous fluid
216 in subduction zones. In partially molten samples, the dihedral angle decreases at high pressures
217 and enhanced water contents (Freitas et al., 2017; Yoshino et al., 2009). The high water contents
218 observed in our melt suggests that hydrous silicate melt produced by the released aqueous fluids
219 from dehydration of amphiboles are efficient in wetting the grain boundaries. The experimental

220 conditions explored in our experiments are likely to produce aqueous fluids and melt dihedral
221 angles that result in excellent inter-connectivity of fluid/melt phase which in turn helps in
222 enhanced electrical conductivity even at lower fluid/melt fractions.

223 We confirmed the partial breakdown of amphibole with detailed electron microprobe
224 analysis, scanning electron microscopy images, and energy-dispersive X-ray spectroscopy
225 (EDS) elemental mapping of recovered samples (**Fig. 4**). The experimental run products
226 indicate dehydration and breakdown of amphibole to secondary mineral phases (**Table 1**). For
227 instance in the experiments (#555), upon dehydration, actinolite completely transforms into a
228 mixture of clinopyroxene (cpx) and orthopyroxene (opx). The orthopyroxene (opx) inherited
229 an amphibole-like elongated form (**Fig. 4b**). In additional experiments (#554, 567, 576), upon
230 dehydration, Fe-kaersutite (#554), hastingsite (#567), and tremolite (#576), transforms to an
231 assemblage consisting of cpx, opx, gt, and secondary amphiboles (**Fig. 4a,c,d**). In addition, we
232 also find relics of pristine or primary amphibole. Relics of pristine amphiboles are often
233 recognizable with SEM images (**Fig. 4**). In all experiments, the dehydration-induced fluids
234 triggered partial melting and crystallized a suite of secondary amphiboles upon a gradual
235 decrease in temperature. The secondary amphiboles showed strong F enrichment and moderate
236 Cl contents compared to the melt phase (**Fig. 5**)

237

238 **4. Discussion**

239 **4.1. Electrical conductivity of the halogen-bearing dehydrating fluid**

240 We observed that the electrical conductivity of halogen bearing fluids is more than a
241 factor of ten or higher compared to the halogen-free aqueous fluids reported in earlier studies
242 (Guo et al., 2011; Manthilake et al., 2016; Wang and Karato, 2013) (**Fig. 6**). Based on the
243 partitioning behavior, it is generally assumed that upon dehydration, F⁻ and Cl⁻ ions in
244 amphibole are readily partitioned into the aqueous fluid phase, making dehydrating fluids in

245 the mantle wedge rich in F and Cl. Because of their highly ionic nature, the aqueous fluids
246 containing halogens are good electrical conductors (Guo & Keppler, 2019; Reynard et al., 2011;
247 Shimojuku et al., 2012, 2014; Sinmyo & Keppler, 2017).

248 Partitioning of halogen between aqueous fluids and anhydrous minerals including
249 olivine and pyroxenes show that Cl and F are dominantly incorporated into the fluid phase
250 (Bernini et al., 2013; Fabbrizio et al., 2013a; Fabbrizio et al., 2013b). However, the chemical
251 analyses of our experimental run products after partial dehydration of amphibole suggest that F
252 and Cl are mostly partitioned into the secondary mineral phases such as edenite and garnet,
253 (**Table 2**). It has been shown that the halogen concentrations in secondary amphiboles in
254 equilibrium with the fluid are lower than the primary amphiboles. (Bernini et al., 2013; Wu &
255 Koga, 2013, 2018). The increase of electrical conductivity of the fluid phase compared to
256 halogen-free fluids can be attributed to the fraction of F and Cl dissolved in the fluid.

257

258 **4.2 Electrical conductivity of hydrous melt**

259 The dehydration-induced hydrous silicate melts produced by ferri-kaersutite, actinolite,
260 hastingsite, and tremolite amphibole compositions, all have electrical conductivities within the
261 range 2-8 S/m. (**Fig. 3**). The electrical conductivity of melt produced by the melting of
262 amphibole in the slab closely resembles the values obtained for basalts commonly found in
263 volcanic-arc settings (Gailler et al., 2019) (**Fig. 6**). This demonstrates that distinguishing the
264 precursor compositions of most hydrous melts based on the electrical conductivity is often
265 challenging and hint towards the broad similarities in electrical charge carrier concentrations in
266 both types of melts.

267 The diverse chemical composition of amphiboles used in this study enables us to
268 investigate the efficiency of charge-carrying cations in hydrous silicate melts (**Fig. 7**). We
269 observe that the increase in the concentrations of Na⁺ and Fe²⁺/Fe³⁺ show strong positive

270 correlation with the electrical conductivity of the melt (**Fig. 7 a,b**). However, we find that an
271 increase in the Ca^{2+} ion concentrations has an inverse effect on electrical conductivity in the
272 melt (**Fig. 7c**). It has been shown that the electrical conductivity and the diffusivity in silicate
273 melts strongly depended on the degree of polymerization (Mills, 1993). The increase of
274 network-breaking Ca^{2+} results in breaking of bonding-oxygen in SiO_4^{4-} tetrahedral and bind
275 with non-bridging oxygen forming both polymerized and depolymerized units (Lee & Stebbins,
276 2006; Maroufi et al., 2016; Mills, 1993). An increase of CaO concentrations affects the number
277 of such anionic units present in the melt (Mills, 1993). The negative correlation observed
278 between the electrical conductivity and the concentration of CaO, could be attributed to the
279 increase of polymerized anions in the melt.

280

281 **4.3 Implications for the wedge-mantle electrical anomalies**

282 The observed electrical conductivity anomalies in subduction zone settings are often
283 linked with the presence of aqueous fluids (McGary et al., 2014). Support for this argument is
284 further reinforced by numerous electrical conductivity studies based on laboratory experiments
285 which demonstrate higher electrical conductivities for aqueous fluid compared to solid mineral
286 phases (Manthilake et al., 2015; Manthilake et al., 2016; Manthilake et al., 2021a; Reynard et
287 al., 2011; Shen et al., 2020; Wang et al., 2012; Wang and Karato, 2013; Zhang et al., 2014).
288 Upon dehydration, the released fluids may lead to the formation of an interconnected network
289 of a conductive phase (fluid/ melt). This interconnected network of highly conductive fluid/melt
290 could dominate the bulk conductivity of rock and mask the relatively resistive matrix made up
291 of remaining mineral phases. Similarly, an interconnected network of fluids/melt also affects
292 the shear modulus of the rock, reducing both compressional and shear wave velocities (Chantel
293 et al., 2016; Freitas et al., 2017, 2019; Manthilake et al., 2021b; Soustelle et al., 2014; Weidner
294 et al., 2018). The concomitant reduction of seismic wave velocities and the seismic attenuation

295 is considered as a strong indication of the presence of a liquid phase. However, given that high
296 electrical conductivities could also be caused by thin films of graphite (Glover, 1996) or
297 crystalline precipitates of metal oxides (Manthilake et al., 2016), a cross-correlation between
298 seismic and electrical signatures are often warranted (Freitas et al., 2019).

299 Several subduction zone settings exhibit elevated electrical conductivity at depths of 40
300 and 100 km in the wedge mantle. Moderate to high electrical conductivity anomalies have been
301 observed in the Cascadia subduction system (CSZ) (Evans et al., 2014; McGary et al., 2014),
302 Cocos subduction system in Sothern Mexico (SM) (Jödicke et al., 2006), Marlborough, New
303 Zealand (NZ) (Wannamaker et al., 2009) Northwestern Costa Rica (CR) (Brasse et al., 2009;
304 Worzewski et al., 2011), Bolivia-Altiplano (BVA) (Brasse et al., 2002), Bolivian Orocline
305 (BVO) (Brasse & Eydam, 2008) and Southern Kyushu (KYU) (Ichiki et al., 2000). These
306 observations of elevated electrical conductivity can often be explained by the presence of
307 aqueous fluid released by dehydration. The depth-dependent MT data from these subduction
308 systems show three clusters of electrical conductivities (**Fig. 8**). Several locations including
309 Northwestern Costa Rica (CR), Sothern Mexico (SM), Marlborough, New Zealand(NZ),
310 Cascadia-Mount Rainier (CAS-MR) (McGary et al., 2014), Sothern Kyushu (Ichiki et al., 2000)
311 exhibits electrical conductivity ~ 0.1 S/m. The second cluster of electrical conductivity ~ 1 S/m
312 is shown by subduction zones including Cascadia-Oregon (CAS-OR) (Evans et al., 2014),
313 Bolivia-Altiplano (BVA) (Brasse et al., 2002). The third cluster of electrical conductivity ~ 1
314 S/m is observed at greater depths 50-100 km, these include Bolivia-Altiplano (BVA) (Brasse
315 et al., 2002), Bolivian Orocline (BVO) (Brasse & Eydam, 2008). The clear distinction between
316 these two shallow clusters could be due to variation in thermal state of the subduction zone, the
317 physical state of the conductive phase, i.e., aqueous fluid, melt/super critical fluids, or
318 conductive solid, and the chemical composition of the conductive phase.

319 Could the observed variation of electrical conductivity between these two states be
320 attributed to the salinity of the aqueous fluids? It is well known that electrical conductivity of
321 ~ 0.1 S/m can be explained by 30 ‰ salinity in aqueous fluids (Manthilake et al., 2016;
322 Shimojuku et al., 2012, 2014; Sinmyo and Keppler, 2017). 30 ‰ salinity is close to the salinity
323 expected at natural seawater. However, electrical conductivity observed for the second cluster
324 i.e., ~ 1 S/m requires fluid with extremely high salinities of more than 100 ‰ (Manthilake et al.,
325 2016). Our study indicates that the high salinities of ~ 100 ‰ may not be achieved in naturally
326 occurring fluids in subduction zones as halogen partitions into thermodynamically stable
327 secondary mineral phases in the downgoing slab (**Table 2**). Naturally occurring fluid inclusions
328 from subduction-related orogenic ophiolites could have salinities up to ~ 89 ‰ salinity
329 (Kawamoto et al., 2018). But this high salinity is rare and only occurs in extreme cases, the
330 average salinity is ~ 45 ‰ (Kawamoto et al., 2018). The expected salinity of our experimental
331 charge, calculated based on the Cl and F partitioned into the fluid phase, is 24 ‰ for Fe
332 kaersutite, 27 ‰ hastingsite, 12 ‰ tremolite, and 0.03 ‰ actinolite. We conclude that the high
333 conductivity anomalies around 0.1 S/m are the range that can be explained by dehydrating fluids
334 exiting from the slab, which contain halogens.

335 The high conductivity anomalies of more than 1 S/m found in subduction systems are
336 located at two distinctive regions relative to the slab (Brasse et al., 2002; Evans et al., 2014;
337 Soyer & Unsworth, 2006). The first location is found at the nose of the mantle wedge in the
338 depth range 20-40 km and shown to have a much smaller spatial distribution (Brasse et al.,
339 2002; Evans et al., 2014; Jödicke et al., 2006; Wannamaker et al., 2009). The second anomaly
340 is located at 60-120 km depths beneath the arc and shows the larger spatial distribution (Brasse
341 et al., 2002; Brasse & Eydam, 2008; Evans et al., 2014; McGary et al., 2014). The anomaly
342 found at the nose of the wedge has been explained by solid conductors such as interconnected
343 magnetite along grain boundaries, which can be precipitated during the dehydration of chlorite

344 (Manthilake et al., 2016). When the electrical anomalies are associated with negative seismic
345 anomalies, such as those found at 60-120 km beneath the arc, an inter-connected liquid must be
346 present in the region. Because the saline fluid in the natural arc setting is not expected to
347 increase the conductivity to 1 S/m, we conclude that a hydrous silicate melt is the likely cause
348 of high conductivity observed at the depth range 60-120 km (**Fig. 8**). If an anomaly is located
349 within the mantle wedge, the partial hydrous silicate melt is likely to be feeding the arc
350 magmatism. If the anomaly is situated near the slab-mantle wedge interface, the partial melt is
351 expected to be that of slab-derived melt, such as partial melting of sediments and/or mafic crust.
352 In either case, small degrees of the partial melt is high in volatile and incompatible elements
353 such as H₂O and Na, and such compositional tendency is consistent with high conductivity
354 (**Fig. 8**).

355

356 **4.4 Implications for the transport of halogen into the deep mantle**

357 Recycling of halogen in the subduction zone settings is directly tied to the aqueous
358 fluids/melts released from the subducting slab. The aqueous fluid is an efficient carrier of easily
359 ionizing halogens, except for F in certain circumstances. Based on the balance of the subduction
360 input and the output from arc volcanoes, nearly all of Cl is recycled back to the surface. In
361 contrast to Cl, more than 90 % of F is estimated to be partitioned to either reservoir located at
362 the wedge mantle or, to deep mantle reservoirs (Straub & Layne, 2003). Experimentally
363 determined partition coefficients also indicate that F is likely to be partitioned to the residual
364 amphibole during dehydration-induced melting (Wu & Koga, 2013).

365 However, both Cl and F can be partitioned to hydrous silicate melts and be effectively
366 removed from the slab, thus increasing F and Cl contents in arc magma (Van den Bleeken and
367 Koga, 2015; Beyer et al. 2016). However, even in the presence of hydrous silicate melt, F is
368 moderately incompatible and can be sequestered in the crystalline structure of minerals

369 including amphibole, mica, and apatite. Thus, some amount of F is expected to be transported
370 into the deep mantle via secondary mineral phases (**Fig. 5**). Because of the distinct partitioning
371 behavior of halogen (F) in melt and aqueous fluids, the efficiency of the halogen recycling is
372 likely to be controlled by the nature of the fluid phase in the subducting slab. This might be
373 further complicated by the presence of supercritical fluids which could enhance the partitioning
374 of elements into the fluids (Kessel et al., 2005). Thus, the injection of halogen into the deep
375 mantle varies greatly from one arc to another depending on the type of liquid coming out of the
376 slab (fluid or slab melt). Our study provided a crucial link between the halogen induced
377 enhanced electrical conductivity of aqueous fluids and melts and also the partitioning of
378 halogen in secondary phases such as amphibole and garnet that could sequester halogens such
379 as F and Cl and transfer them to the deep Earth. Once halogen is subducted into the transition
380 zone and lower mantle, the high-pressure phases can accommodate these elements in its
381 crystalline structure and it is not expected to produce significant fractionation during the mantle
382 convection.

383 Variable degrees of halogen recycling has already been inferred based on the
384 distribution of halogens in ocean island basalts. Much of the variations of Cl and F abundances
385 are often attributed to near-surface contamination (Kendrick et al., 2015). However, there are
386 variations in the concentration of halogens that could be attributed to the variations related to
387 the source of the OIBs (Kovalenko et al., 2006; Jackson et al., 2015; Rose-Koga et al., 2017;
388 Hanyu et al., 2019; Kendrick et al. 2015). An increase of F in ocean island basalts compared to
389 a MORB source mantle appears to correlate with the radiogenic Pb signature establishing the
390 direct relationship between recycling slab and F enrichment (Rose-Koga et al., 2017).

391

392 **Acknowledgments**

393 We thank J-M Henot (deceased) and E. Voyer for help with the SEM analyses, J-L
394 Davidal for the electron microprobe analyses, and Antoine Mathieu for the technical assistance.
395 Christian Nicollet is thanked for providing some natural amphiboles. GM acknowledges
396 funding from the INSU-CNRS. M.M. is supported by the US National Science Foundation
397 grants, EAR 1753125, 1763215. This research was financed by the French Government
398 Laboratory of Excellence initiative n°ANR-10-LABX-0006, the Région Auvergne, and the
399 European Regional Development Fund (ClerVolc contribution number 454). The authors
400 comply with AGU's data policy, and the data of this study are available in Zonodo ([http://](http://doi.org/10.5281/zenodo.4267663)
401 doi.org/10.5281/zenodo.4267663). The authors declare no competing financial interests.

402

403

404 **References**

- 405 Bernini, D., Wiedenbeck, M., Dolejš, D., & Keppler, H. (2013). Partitioning of halogens
406 between mantle minerals and aqueous fluids: Implications for the fluid flow regime in
407 subduction zones. *Contributions to Mineralogy and Petrology*, *165*(1), 117–128.
408 <https://doi.org/10.1007/s00410-012-0799-4>
- 409 Beyer, C., Klemme, S., Wiedenbeck, M., Stracke, A., & Vollmer, C. (2012). Fluorine in
410 nominally fluorine-free mantle minerals: Experimental partitioning of F between olivine,
411 orthopyroxene and silicate melts with implications for magmatic processes. *Earth and*
412 *Planetary Science Letters*, *337–338*, 1–9. <https://doi.org/10.1016/j.epsl.2012.05.003>
- 413 Beyer, C., Klemme, S., Grützner, T., Ireland, T. R., Magee, C. W., & Frost, D. J. (2016).
414 Fluorine partitioning between eclogitic garnet, clinopyroxene, and melt at upper mantle
415 conditions. *Chemical Geology*, *437*, 88–97.
416 <https://doi.org/10.1016/j.chemgeo.2016.05.032>

- 417 Van den Bleeken, G., & Koga, K. T. (2015). Experimentally determined distribution of
418 fluorine and chlorine upon hydrous slab melting, and implications for F-Cl cycling
419 through subduction zones. *Geochimica et Cosmochimica Acta*, *171*, 353–373.
420 <https://doi.org/10.1016/j.gca.2015.09.030>
- 421 Brasse, H., & Eydam, D. (2008). Electrical conductivity beneath the Bolivian Orocline and its
422 relation to subduction processes at the South American continental margin. *Journal of*
423 *Geophysical Research: Solid Earth*, *113*(7), 1–14.
424 <https://doi.org/10.1029/2007JB005142>
- 425 Brasse, H., Lezaeta, P., Rath, V., Schwalenberg, K., Soyer, W., & Haak, V. (2002). The
426 Bolivian Altiplano conductivity anomaly. *Journal of Geophysical Research-Solid Earth*,
427 *107*(B5), 17. <https://doi.org/2096> Artn 2096
- 428 Brasse, H., Kapinos, G., Mütschard, L., Alvarado, G. E., Worzewski, T., & Jegen, M. (2009).
429 Deep electrical resistivity structure of northwestern Costa Rica. *Geophysical Research*
430 *Letters*, *36*(2), 1–5. <https://doi.org/10.1029/2008GL036397>
- 431 Brenan, J. M. (1993). Diffusion of chlorine in fluid-bearing quartzite: effects of fluid
432 composition and total porosity. *Contributions to Mineralogy and Petrology*, *115*(2),
433 215–224. <https://doi.org/10.1007/BF00321221>
- 434 Chantel, J., Manthilake, G., Andrault, D., Novella, D., Yu, T., & Wang, Y. (2016).
435 Experimental evidence supports mantle partial melting in the asthenosphere. *Science*
436 *Advances*, *2*(5), e1600246. <https://doi.org/10.1126/sciadv.1600246>
- 437 Dalou, C., Koga, K. T., Shimizu, N., Boulon, J., & Devidal, J. L. (2012). Experimental
438 determination of F and Cl partitioning between lherzolite and basaltic melt.
439 *Contributions to Mineralogy and Petrology*, *163*(4), 591–609.
440 <https://doi.org/10.1007/s00410-011-0688-2>
- 441 Dalou, C., Koga, K. T., Le Voyer, M., & Shimizu, N. (2014). Contrasting partition behavior

442 of F and Cl during hydrous mantle melting: implications for Cl/F signature in arc
443 magmas. *Progress in Earth and Planetary Science*, 1(1), 1–17.
444 <https://doi.org/10.1186/s40645-014-0026-1>

445 Debret, B., Koga, K. T., Cattani, F., Nicollet, C., Van den Bleeken, G., & Schwartz, S. (2016).
446 Volatile (Li, B, F and Cl) mobility during amphibole breakdown in subduction zones.
447 *Lithos*, 244, 165–181. <https://doi.org/10.1016/j.lithos.2015.12.004>

448 Evans, R. L., Wannamaker, P. E., McGary, R. S., & Elsenbeck, J. (2014). Electrical structure
449 of the central Cascadia subduction zone: The EMSLAB Lincoln Line revisited. *Earth
450 and Planetary Science Letters*, 402(C), 265–274.
451 <https://doi.org/10.1016/j.epsl.2013.04.021>

452 Fabbriozio, A., Stalder, R., Hametner, K., & Günther, D. (2013). Experimental chlorine
453 partitioning between forsterite, enstatite and aqueous fluid at upper mantle conditions.
454 *Geochimica et Cosmochimica Acta*, 121, 684–700.
455 <https://doi.org/10.1016/j.gca.2013.05.026>

456 Fabbriozio, A., Stalder, R., Hametner, K., Günther, D., & Marquardt, K. (2013). Experimental
457 partitioning of halogens and other trace elements between olivine, pyroxenes, amphibole
458 and aqueous fluid at 2 GPa and 900–1,300 °C. *Contributions to Mineralogy and
459 Petrology*, 166(2), 639–653. <https://doi.org/10.1007/s00410-013-0902-5>

460 Foley, S. (1991). High-pressure stability of the fluor- and hydroxy-endmembers of pargasite
461 and K-richterite. *Geochimica et Cosmochimica Acta*, 55(9), 2689–2694.
462 [https://doi.org/10.1016/0016-7037\(91\)90386-J](https://doi.org/10.1016/0016-7037(91)90386-J)

463 Freitas, D., & Manthilake, G. (2019). Electrical conductivity of hydrous silicate melts :
464 Implications for the bottom-up hydration of Earth ' s upper mantle. *Earth and Planetary
465 Science Letters*, 523, 115712. <https://doi.org/10.1016/j.epsl.2019.115712>

466 Freitas, D., Manthilake, G., Schiavi, F., Chantel, J., Bolfan-Casanova, N., Bouhifd, M. A., &

- 467 Andrault, D. (2017). Experimental evidence supporting a global melt layer at the base of
468 the Earth's upper mantle. *Nature Communications*, 8(1), 2186.
469 <https://doi.org/10.1038/s41467-017-02275-9>
- 470 Freitas, D., Manthilake, G., Chantel, J., Bouhifd, M. A., & Andrault, D. (2019). Simultaneous
471 measurements of electrical conductivity and seismic wave velocity of partially molten
472 geological materials: effect of evolving melt texture. *Physics and Chemistry of Minerals*,
473 46(6), 535–551. <https://doi.org/10.1007/s00269-019-01021-5>
- 474 Frost, B. R. (1991). Introduction to oxygen fugacity and its petrologic importance. In D. .
475 Lindsley (Ed.), *Reviews in Mineralogy: Oxide Minerals: Petrologic and Magnetic*
476 *Significance* (pp. 1–9).
- 477 Gailler, L., Kauahikaua, J., Lénat, J. J.-F., Revil, A., Gresse, M., Ahmed, A. S., et al. (2019).
478 3D electrical conductivity imaging of Halema'uma'u lava lake (Kīlauea volcano).
479 *Journal of Volcanology and Geothermal Research*.
480 <https://doi.org/10.1016/j.jvolgeores.2019.06.001>
- 481 Guo, H., & Keppler, H. (2019). Electrical Conductivity of NaCl-Bearing Aqueous Fluids to
482 900 °C and 5 GPa. *Journal of Geophysical Research: Solid Earth*, 124(2), 1397–1411.
483 <https://doi.org/10.1029/2018JB016658>
- 484 Guo, X., Yoshino, T., & Katayama, I. (2011). Electrical conductivity anisotropy of deformed
485 talc rocks and serpentinites at 3GPa. *Physics of the Earth and Planetary Interiors*,
486 188(1–2), 69–81. <https://doi.org/10.1016/j.pepi.2011.06.012>
- 487 Guo, X., Yoshino, T., & Shimojuku, A. (2015). Electrical conductivity of albite-(quartz)-
488 water and albite-water-NaCl systems and its implication to the high conductivity
489 anomalies in the continental crust. *Earth and Planetary Science Letters*, 412, 1–9.
490 <https://doi.org/10.1016/j.epsl.2014.12.021>
- 491 Hanyu, T., Shimizu, K., Ushikubo, T., Kimura, J. I., Chang, Q., Hamada, M., et al. (2019).

492 Tiny droplets of ocean island basalts unveil Earth's deep chlorine cycle. *Nature*
493 *Communications*, 10(60), 1–7. <https://doi.org/10.1038/s41467-018-07955-8>

494 Holloway, J. R., & Ford, C. E. (1975). Fluid-absent melting of the fluoro-hydroxy amphibole
495 pargasite to 35 kilobars. *Earth and Planetary Science Letters*, 25(1), 44–48.
496 [https://doi.org/10.1016/0012-821X\(75\)90208-3](https://doi.org/10.1016/0012-821X(75)90208-3)

497 Ichiki, M., Sumitomo, N., & Kagiya, T. (2000). Resistivity structure of high-angle
498 subduction zone in the southern Kyushu district, southwestern Japan. *Earth, Planets and*
499 *Space*, 52(8), 539–548. <https://doi.org/10.5636/eps.52.539>

500 Ito, E., Harris, D. M., & Anderson, A. T. (1983). Alteration of oceanic crust and geologic
501 cycling of chlorine and water. *Geochimica et Cosmochimica Acta*, 47(9), 1613–1624.
502 [https://doi.org/10.1016/0016-7037\(83\)90188-6](https://doi.org/10.1016/0016-7037(83)90188-6)

503 Jackson, M. G., Koga, K., Price, A. A., Konter, J. G., Koppers, A. A. P., Finlayson, V. ., et al.
504 (2015). Deeply dredged submarine HIMU glasses from the Tuvalu Islands, Polynesia:
505 Implications for volatile budgets of recycled oceanic crust. *Geochemistry, Geophysics,*
506 *Geosystems*, 16, 3210–3234. <https://doi.org/10.1002/2015GC005966>

507 Jödicke, H., Jording, A., Ferrari, L., Arzate, J., Mezger, K., & Rüpke, L. (2006). Fluid release
508 from the subducted Cocos plate and partial melting of the crust deduced from
509 magnetotelluric studies in southern Mexico: Implications for the generation of volcanism
510 and subduction dynamics. *Journal of Geophysical Research: Solid Earth*, 111(8), 1–22.
511 <https://doi.org/10.1029/2005JB003739>

512 Kawamoto, T., Hertwig, A., Schertl, H. P., & Maresch, W. V. (2018). Fluid inclusions in
513 jadeitite and jadeite-rich rock from serpentinite mélanges in northern Hispaniola:
514 Trapped ambient fluids in a cold subduction channel. *Lithos*, 308–309, 227–241.
515 <https://doi.org/10.1016/j.lithos.2018.02.024>

516 Kendrick, M. A., Scambelluri, M., Honda, M., & Phillips, D. (2011). High abundances of

517 noble gas and chlorine delivered to the mantle by serpentinite subduction. *Nature*
518 *Geoscience*, 4(11), 807–812. <https://doi.org/10.1038/ngeo1270>

519 Kendrick, M. A., Jackson, M. G., Hauri, E. H., & Phillips, D. (2015). The halogen (F, Cl, Br,
520 I) and H₂O systematics of Samoan lavas: Assimilated-seawater, EM2 and high-³He/⁴He
521 components. *Earth and Planetary Science Letters*, 410, 197–209.
522 <https://doi.org/10.1016/j.epsl.2014.11.026>

523 Kessel, R., Schmidt, M. W., Ulmer, P., & Pettke, T. (2005). Trace element signature of
524 subduction-zone fluids, melts and supercritical liquids at 120-180 km depth. *Nature*,
525 437(7059), 724–727. <https://doi.org/10.1038/nature03971>

526 Kovalenko, V. I., Naumov, V. B., Girnis, A. V., Dorofeeva, V. A., & Yarmolyuk, V. V.
527 (2006). Composition and chemical structure of oceanic mantle plumes. *Petrology*, 14(5),
528 452–476. <https://doi.org/10.1134/S0869591106050031>

529 Lee, S. K., & Stebbins, J. F. (2006). Disorder and the extent of polymerization in calcium
530 silicate and aluminosilicate glasses: O-17 NMR results and quantum chemical molecular
531 orbital calculations. *Geochimica et Cosmochimica Acta*, 70(16), 4275–4286.
532 <https://doi.org/10.1016/j.gca.2006.06.1550>

533 Locock, A. J. (2014). An Excel spreadsheet to classify chemical analyses of amphiboles
534 following the IMA 2012 recommendations. *Computers and Geosciences*, 62, 1–11.
535 <https://doi.org/10.1016/j.cageo.2013.09.011>

536 Mandler, B. E., & Grove, T. L. (2016). Controls on the stability and composition of
537 amphibole in the Earth's mantle. *Contributions to Mineralogy and Petrology*, 171(8–9),
538 1–20. <https://doi.org/10.1007/s00410-016-1281-5>

539 Manthilake, G, Bolfan-Casanova, N., Novella, D., Mookherjee, M., & Andrault, D. (2016).
540 Dehydration of chlorite explains anomalously high electrical conductivity in the mantle
541 wedges. *Science Advances*, 2(5). <https://doi.org/10.1126/sciadv.1501631>

542 Manthilake, G., Mookherjee, M., & Miyajima, N. (2021a). Insights on the deep carbon cycle
543 from the electrical conductivity of carbon-bearing aqueous fluids. *Scientific Reports*.
544 <https://doi.org/10.1038/s41598-021-82174-8>

545 Manthilake, G, Chantel, J., Guignot, N., & King, A. (2021b). The Anomalous Seismic
546 Behavior of Aqueous Fluids Released during Dehydration of Chlorite in Subduction
547 Zones. *Minerals*, 11(70). <https://doi.org/10.3390/min11010070>

548 Manthilake, Geeth, Mookherjee, M., Bolfan-Casanova, N., & Andrault, D. (2015). Electrical
549 conductivity of lawsonite and dehydrating fluids at high pressures and temperatures.
550 *Geophysical Research Letters*, 42(18), 7398–7405.
551 <https://doi.org/10.1002/2015GL064804>

552 Maroufi, S., Amini, S., Jahanshahi, S., & Ostrovski, O. (2016). Diffusion Coefficients and
553 Structural Parameters of Molten Slags. In *Advances in Molten Slags, Fluxes, and Salts*
554 (pp. 493–500). John Wiley & Sons, Ltd. <https://doi.org/10.1002/9781119333197.ch52>

555 Mathez, E. A., & Webster, J. D. (2005). Partitioning behavior of chlorine and fluorine in the
556 system apatite-silicate melt-fluid. *Geochimica et Cosmochimica Acta*, 69(5), 1275–1286.
557 <https://doi.org/10.1016/j.gca.2004.08.035>

558 McGary, R. S., Evans, R. L., Wannamaker, P. E., Elsenbeck, J., & Rondenay, S. (2014).
559 Pathway from subducting slab to surface for melt and fluids beneath Mount Rainier.
560 *Nature*, 511(7509), 338–340. <https://doi.org/10.1038/nature13493>

561 Mibe, K., Fujii, T., & Yasuda, A. (1999). Control of the location of the volcanic front in
562 island arcs by aqueous fluid connectivity in the mantle wedge. *Nature*, 401(6750), 259–
563 262. <https://doi.org/10.1038/45762>

564 Mills, K. C. (1993). The Influence of Structure on the Physico-chemical Properties of Slags.
565 *Isij International*, 33(1), 148–155. <https://doi.org/10.2355/isijinternational.33.148>

566 Mitchell, a. C., & Nellis, W. J. (1982). Equation of state and electrical conductivity of water

567 and ammonia shocked to the 100 GPa (1 Mbar) pressure range. *The Journal of Chemical*
568 *Physics*, 76(12), 6273–6281. <https://doi.org/10.1063/1.443030>

569 Ni, H., Keppler, H., & Behrens, H. (2011). Electrical conductivity of hydrous basaltic melts:
570 Implications for partial melting in the upper mantle. *Contributions to Mineralogy and*
571 *Petrology*, 162(3), 637–650. <https://doi.org/10.1007/s00410-011-0617-4>

572 Reynard, B., Mibe, K., & de Moortèle, B. Van. (2011). Electrical conductivity of the
573 serpentinised mantle and fluid flow in subduction zones. *Earth and Planetary Science*
574 *Letters*, 307(3–4), 387–394. <https://doi.org/10.1016/j.epsl.2011.05.013>

575 Roberge, M., Bureau, H., Bolfan-Casanova, N., Raepsaet, C., Surble, S., Khodja, H., et al.
576 (2017). Chlorine in wadsleyite and ringwoodite: An experimental study. *Earth and*
577 *Planetary Science Letters*, 467, 99–107. <https://doi.org/10.1016/j.epsl.2017.03.025>

578 Rose-Koga, E. F., Koga, K. T., Moreira, M., Vlastelic, I., Jackson, M. G., Whitehouse, M. J.,
579 et al. (2017). Geochemical systematics of Pb isotopes, fluorine, and sulfur in melt
580 inclusions from São Miguel, Azores. *Chemical Geology*, 458, 22–37.
581 <https://doi.org/10.1016/j.chemgeo.2017.03.024>

582 Rose-Koga, E. F., Koga, K. T., Devidal, J. L., Shimizu, N., Voyer, M. Le, Dalou, C., &
583 Döbeli, M. (2020). In-situ measurements of magmatic volatile elements, F, S, and Cl, by
584 electron microprobe, secondary ion mass spectrometry, and heavy ion elastic recoil
585 detection analysis. *American Mineralogist*, 105(5), 616–626. [https://doi.org/10.2138/am-](https://doi.org/10.2138/am-2020-7221)
586 [2020-7221](https://doi.org/10.2138/am-2020-7221)

587 Sakuma, H., & Ichiki, M. (2016). Electrical conductivity of NaCl-H₂O fluid in the crust.
588 *Journal of Geophysical Research B: Solid Earth*, 121(2), 577–594.
589 <https://doi.org/10.1002/2015JB012219>

590 Scambelluri, M., Müntener, O., Ottolini, L., Pettke, T. T., & Vannucci, R. (2004). The fate of
591 B, Cl and Li in the subducted oceanic mantle and in the antigorite breakdown fluids.

592 *Earth and Planetary Science Letters*, 222(1), 217–234.
593 <https://doi.org/10.1016/j.epsl.2004.02.012>

594 Schmidt, M. W., & Poli, S. (1998). Experimentally based water budgets for dehydrating slabs
595 and consequences for arc magma generation. *Earth and Planetary Science Letters*,
596 163(1–4), 361–379. [https://doi.org/10.1016/S0012-821X\(98\)00142-3](https://doi.org/10.1016/S0012-821X(98)00142-3)

597 Shen, K., Wang, D., & Liu, T. (2020). Electrical conductivity of tremolite under high
598 temperature and pressure: implications for the high-conductivity anomalies in the Earth
599 and Venus. *Contributions to Mineralogy and Petrology*, 175(5), 1–12.
600 <https://doi.org/10.1007/s00410-020-01688-y>

601 Shimojuku, A., Yoshino, T., Yamazaki, D., & Okudaira, T. (2012). Electrical conductivity of
602 fluid-bearing quartzite under lower crustal conditions. *Physics of the Earth and*
603 *Planetary Interiors*, 198–199, 1–8. <https://doi.org/10.1016/j.pepi.2012.03.007>

604 Shimojuku, A., Yoshino, T., & Yamazaki, D. (2014). Electrical conductivity of brine-bearing
605 quartzite at 1 GPa: implications for fluid content and salinity of the crust. *Earth, Planets*
606 *and Space*, 66(1), 2. <https://doi.org/10.1186/1880-5981-66-2>

607 Sinmyo, R., & Keppler, H. (2017). Electrical conductivity of NaCl-bearing aqueous fluids to
608 600 °C and 1 GPa. *Contributions to Mineralogy and Petrology*, 172(1), 1–12.
609 <https://doi.org/10.1007/s00410-016-1323-z>

610 Soustelle, V., Walte, N. P., Manthilake, M. A. G. M., & Frost, D. J. (2014). Melt migration
611 and melt-rock reactions in the deforming Earth’s upper mantle: Experiments at high
612 pressure and temperature. *Geology*, 42(1), 83–86. <https://doi.org/10.1130/G34889.1>

613 Soyer, W., & Unsworth, M. (2006). Deep electrical structure of the northern Cascadia (British
614 Columbia, Canada) subduction zone: Implications for the distribution of fluids. *Geology*,
615 34(1), 53–56. <https://doi.org/10.1130/G21951.1>

616 Straub, S. M., & Layne, G. D. (2003). Decoupling of fluids and fluid-mobile elements during

617 shallow subduction: Evidence from halogen-rich andesite melt inclusions from the Izu
618 arc volcanic front. *Geochemistry, Geophysics, Geosystems*, 4(7).
619 <https://doi.org/10.1029/2002GC000349>

620 Wallace, P. J. (2005). Volatiles in subduction zone magmas: Concentrations and fluxes based
621 on melt inclusion and volcanic gas data. *Journal of Volcanology and Geothermal*
622 *Research*, 140(1–3), 217–240. <https://doi.org/10.1016/j.jvolgeores.2004.07.023>

623 Wang, D., & Karato, S. ichiro. (2013). Electrical conductivity of talc aggregates at 0.5 GPa:
624 Influence of dehydration. *Physics and Chemistry of Minerals*, 40(1), 11–17.
625 <https://doi.org/10.1007/s00269-012-0541-9>

626 Wang, D., Guo, Y., Yu, Y., & Karato, S. ichiro. (2012). Electrical conductivity of amphibole-
627 bearing rocks: Influence of dehydration. *Contributions to Mineralogy and Petrology*,
628 164(1), 17–25. <https://doi.org/10.1007/s00410-012-0722-z>

629 Wannamaker, P. E., Caldwell, T. G., Jiracek, G. R., Maris, V., Hill, G. J., Ogawa, Y., et al.
630 (2009). Fluid and deformation regime of an advancing subduction system at
631 Marlborough, New Zealand. *Nature*, 460(7256), 733–736.
632 <https://doi.org/10.1038/nature08204>

633 Webster, J. D., Tappen, C. M., & Mandeville, C. W. (2009). Partitioning behavior of chlorine
634 and fluorine in the system apatite-melt-fluid. II: Felsic silicate systems at 200 MPa.
635 *Geochimica et Cosmochimica Acta*, 73(3), 559–581.
636 <https://doi.org/10.1016/j.gca.2008.10.034>

637 Weidner, D. J., Li, L., Whitaker, M. L., & Triplett, R. (2018). Ultrasonic Acoustic Velocities
638 During Partial Melting of a Mantle Peridotite KLB-1. *Journal of Geophysical Research:*
639 *Solid Earth*, 123(2), 1252–1261. <https://doi.org/10.1002/2017JB014753>

640 Worzewski, T., Jegen, M., Kopp, H., Brasse, H., & Taylor Castillo, W. (2011).
641 Magnetotelluric image of the fluid cycle in the Costa Rican subduction zone. *Nature*

642 *Geoscience*, 4(2), 108–111. <https://doi.org/10.1038/ngeo1041>

643 Wu, J., & Koga, K. T. (2013). Fluorine partitioning between hydrous minerals and aqueous
644 fluid at 1GPa and 770-947°C: A new constraint on slab flux. *Geochimica et*
645 *Cosmochimica Acta*, 119, 77–92. <https://doi.org/10.1016/j.gca.2013.05.025>

646 Wu, J., & Koga, K. T. (2018). Direct analyses of fluorine in aqueous fluids extracted from 1-
647 GPa experiments. *Chemical Geology*, 502, 44–54.
648 <https://doi.org/10.1016/j.chemgeo.2018.10.011>

649 Wyllie, P. J., & Wolf, M. B. (1993). Amphibolite dehydration-melting: Sorting out the
650 solidus. *Geological Society Special Publication*, 76(76), 405–416.
651 <https://doi.org/10.1144/GSL.SP.1993.076.01.20>

652 Yoshino, T., & Jaseem, V. (2018). Fluorine solubility in bridgmanite: A potential fluorine
653 reservoir in the Earth’s mantle. *Earth and Planetary Science Letters*, 504, 106–114.
654 <https://doi.org/10.1016/j.epsl.2018.10.009>

655 Yoshino, T., Mibe, K., Yasuda, A., & Fujii, T. (2002). Wetting properties of anorthite
656 aggregates: Implications for fluid connectivity in continental lower crust. *Journal of*
657 *Geophysical Research: Solid Earth*, 107(B1), ECV 10-1-ECV 10-8.
658 <https://doi.org/10.1029/2001jb000440>

659 Yoshino, T., Yamazaki, D., & Mibe, K. (2009). Well-wetted olivine grain boundaries in
660 partially molten peridotite in the asthenosphere. *Earth and Planetary Science Letters*,
661 283(1–4), 167–173. <https://doi.org/10.1016/j.epsl.2009.04.007>

662 Zhang, B., Yoshino, T., Yamazaki, D., Manthilake, G., & Katsura, T. (2014). Electrical
663 conductivity anisotropy in partially molten peridotite under shear deformation. *Earth and*
664 *Planetary Science Letters*, 405, 98–109. <https://doi.org/10.1016/j.epsl.2014.08.018>

665

666

667 **Figure captions**

668 **Figure 1. (a)** Schematic cross-section of the high-pressure cell-assembly used for the electrical
669 conductivity measurements. The backscattered electron (BSE) images of (b) Fe kaersutite, (c)
670 actinolite, (d) hastingsite, (e) tremolite. The BSE images were acquired after the electrical
671 conductivity measurements.

672

673 **Figure 2.** Cole-cole plot of actinolite sample with increasing temperature. (a) At temperatures
674 below dehydration (673 K), conduction is through minerals in solid-state. The conductivity of
675 the solid mineral grains could be modeled with an R-CPE circuit, with a phase angle of 15.5
676 degrees. (b) At 841 K, the impedance spectrum shows the development of an inductive loop in
677 response to the onset of dehydration. The equivalent circuit can be represented as an R-CPE
678 with inductive component L. The induction at low frequencies may due to the adsorption of
679 ionic species in the electrode surface or erosion of electrodes due to fluid phases. (c) Further
680 increase in temperature to 1258 K results in a sudden decrease in sample resistance. The
681 persisting induction in impedance spectra indicates a possible reaction of melt with Ni
682 electrodes.

683

684 **Figure 3.** A plot of electrical conductivity of amphibole as a function of reciprocal temperature.
685 The symbols, blue, black, and red indicate solid, fluid, and melt, respectively. Activation
686 enthalpies below dehydrating temperatures are indicated in eV, next to individual fits. The
687 vertical lines indicate possible dehydration / melting temperatures for each mineral phase. The
688 uncertainties in electrical conductivity result from the estimations of temperature, pressure,
689 sample dimensions and data fitting errors and are estimated to be less than 5 %. Error bars are
690 smaller than the size of the markers.

691

692 **Figure 4.** Electron back-scattered image and the corresponding energy-dispersive X-ray
693 spectroscopy (EDS) chemical map amphibole sample after the electrical conductivity
694 measurements. (a) BSE image of exp. 554 Fe-Kaersutite breakdown. (b) Result of phase
695 identification. P1 (red) is the remains of the initial Fe-Kaersutite, P2 (green) is garnet, P3 (blue)
696 is the secondary garnet, P4 (light blue) is olivine but it appears to be metastable intermediate
697 composition, P5 (purple) is porosity. (c) BSE image of exp. 555 actinolite breakdown showing
698 porous texture with a bi-phase assembly. (d) Result of phase identification analysis. P1 (red) is
699 cpx, P2 (green) is opx, and P3 (blue) corresponds to a high porosity zone with a high Cl signal.
700 (e) BSE image of exp. 567 hastingsite breakdown. This starting material had some inclusions
701 in the picked crystal, resulting in a larger number of phases in the charge. (f) Result of phase
702 identification. P1 (red) indicates amphiboles, but it was not possible to distinguish the initial
703 and secondary amphibole, as their compositional change was subtle. P2 (green) is opx. P3 (blue)
704 is melt. P4 (light blue) is magnetite. P5 (purple) is ilmenite. P6 (yellow) is calcite. P7 (orange)
705 is isolated tiny dots, which are the noise of EDS image. (g) BSE image of exp. 576 tremolite
706 breakdown showing a porous texture. (h) Result of phase identification is shown in colors. P1
707 (red) remains of the initial tremolite, P2 (green) is the secondary amphibolite, fluoro-edenite.
708 P3 (blue) is opx in needle form. Note opx and cpx are included in poikilitic fluoro-edenite. P4
709 (light blue) is melt. P5 (purple) corresponds to the high porosity zone.

710

711 **Figure 5.** A compilation of electrical conductivity data of hydrous minerals, dehydrating fluids,
712 and hydrous melt. The vertical lines represent arbitrary boundaries defined based on talc (tlc)
713 (Guo et al., 2011; Wang & Karato, 2013), serpentine (serp) (Reynard et al., 2011), chlorite (chl)
714 (Manthilake et al., 2016) and amp (this study) and there dehydrating products. The electrical
715 conductivity of saline fluids, basaltic melt (Gailler et al., 2019; Ni et al., 2011) and magnetite
716 precipitates (Manthilake et al., 2016) are shown for comparison.

717

718 **Figure 6.** The energy-dispersive X-ray spectroscopy (EDS) chemical map showing the F
719 concentrations of tremolite samples after dehydration. The F is mostly incorporated into the
720 secondary fluoro-edenite (Ed) (green shades). The hydrous melt is shown in blue.

721

722 **Figure 7.** A plot of the logarithm of electrical conductivity of melt as a function of the Na₂O,
723 FeO, and CaO wt % in the melt. Solid lines represent linear fits through data points with
724 $(1.0927 \pm 2.7093) + (1.171 \pm 0.7342)x$ for Na₂O, $(1.9912 \pm 1.6585) + (0.503331 \pm$
725 $0.23433)x$ for FeO, and $(5.2806 \pm 5.7038) - (0.11349 \pm 0.52924)x$ for CaO. The
726 electrical conductivities of melt were taken at the highest temperature of each experiment.

727

728 **Figure 8.** Electrical conductivity of a variety of fluid and melt compared with the range of
729 values reported for subduction zones. The electrical conductivity presented in the figure are
730 from the Cascadia subduction system (Evans et al., 2014; Soyer & Unsworth, 2006), Cocos
731 subduction system in Sothern Mexico (Jödicke et al., 2006), Marlborough, New Zealand
732 (Wannamaker et al., 2009) Northwestern Costa Rica (Brasse et al., 2009; Worzewski et al.,
733 2011), Bolivia-Altiplano (Brasse et al., 2002), Bolivian Orocline (Brasse & Eydam, 2008) and
734 Southern Kyushu (Ichiki et al., 2000).

735

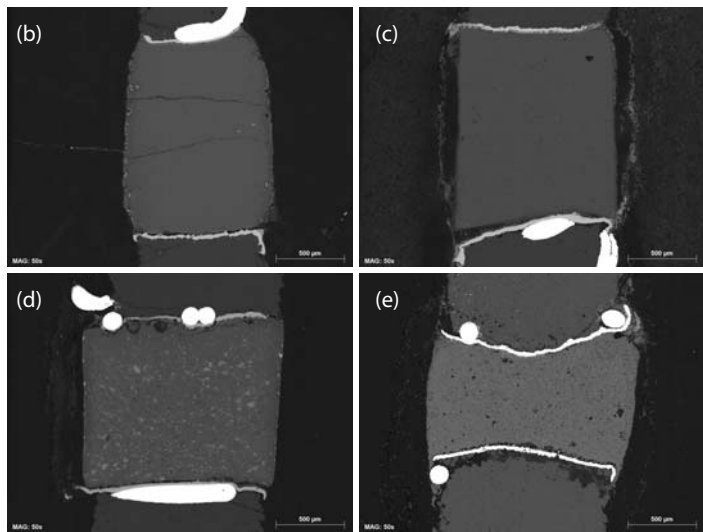
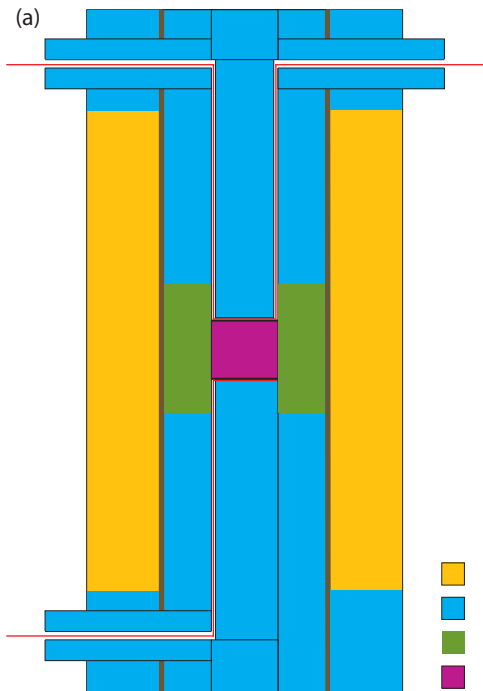
736

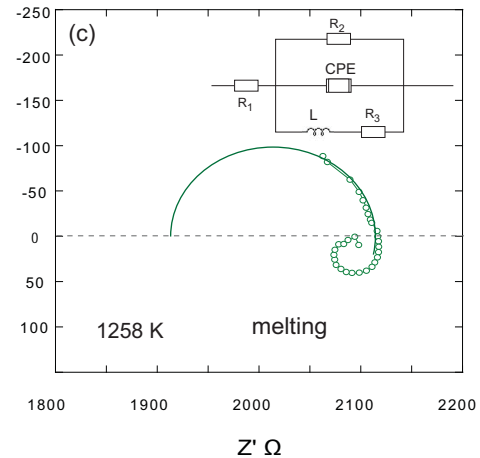
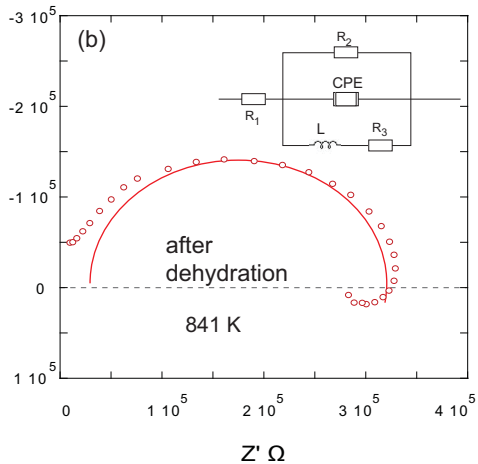
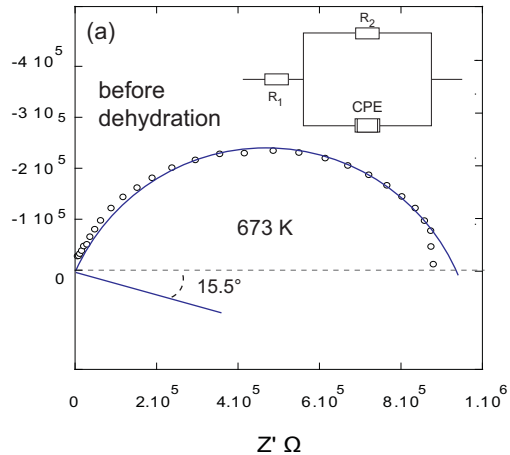
737 **List of tables.**

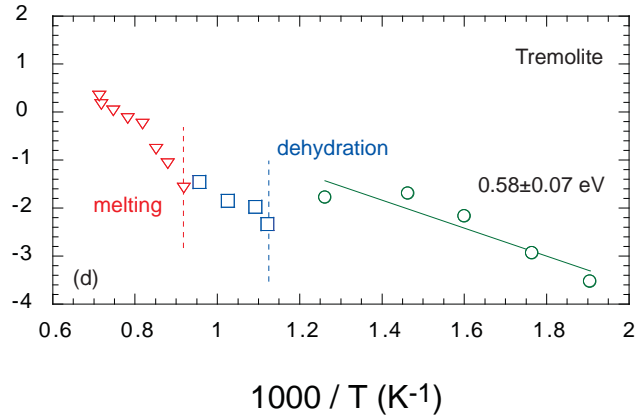
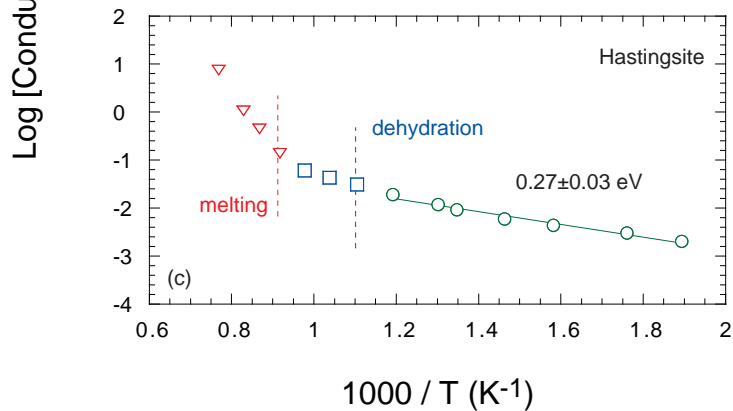
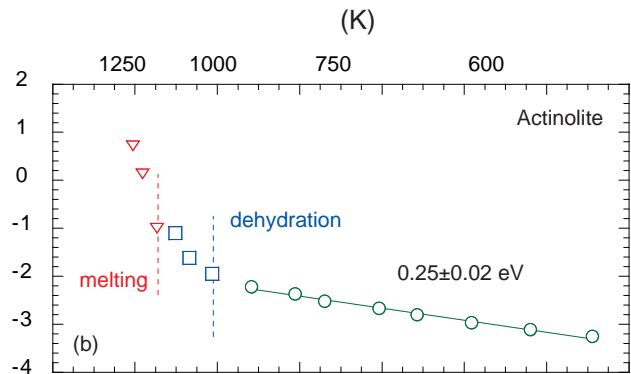
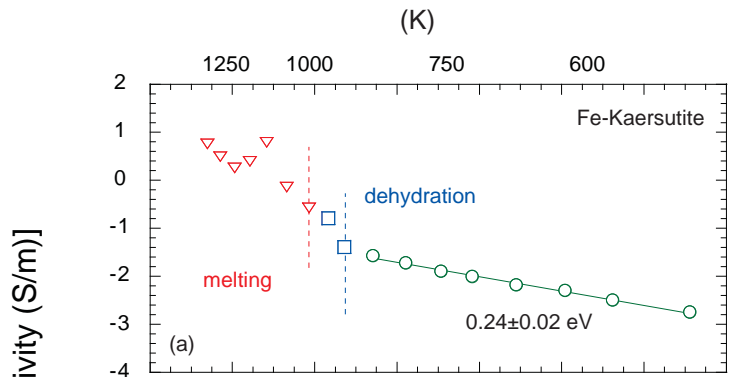
738 **Table 1.** Pressures and temperatures explored in this study and the resulting phases including
739 secondary mineral phases, fluids, and melts.

740

741 **Table 2.** Chemistry of the primary amphiboles and the secondary mineral phases produced after
742 dehydration and dehydration melting.



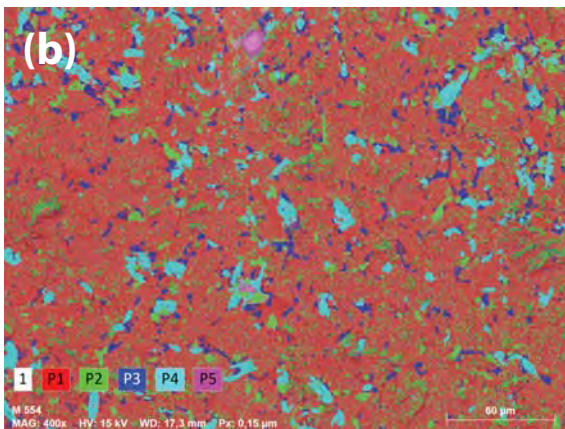
$Z'' \Omega$ 



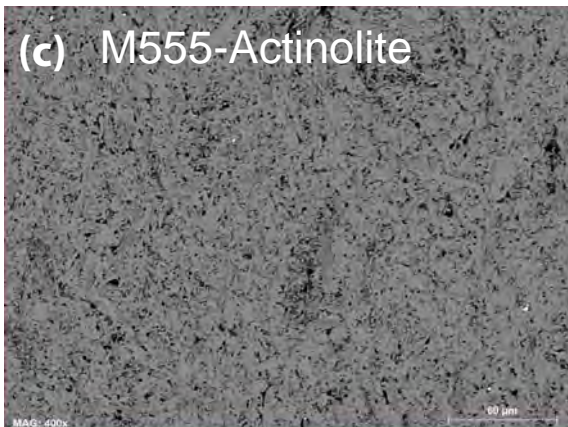
(a) M554-Fe Kaersutite



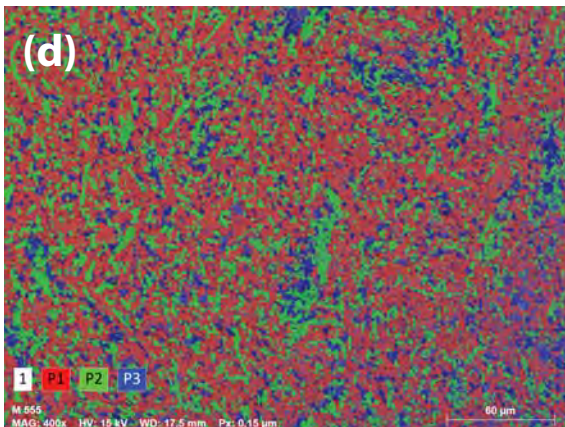
(b)



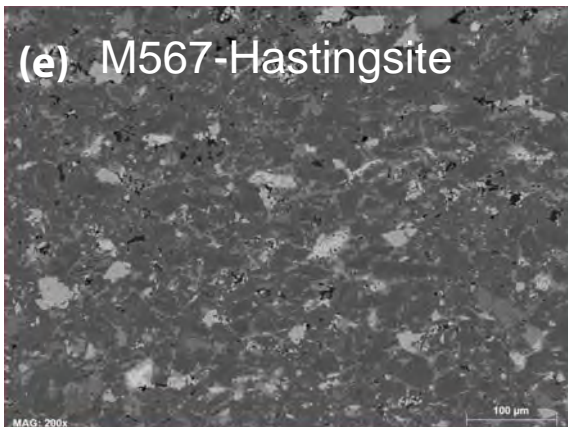
(c) M555-Actinolite



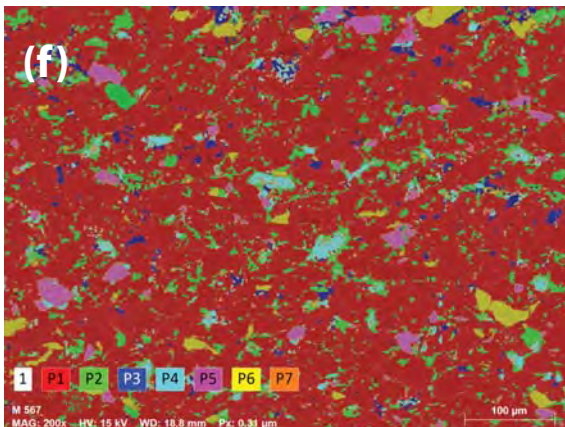
(d)



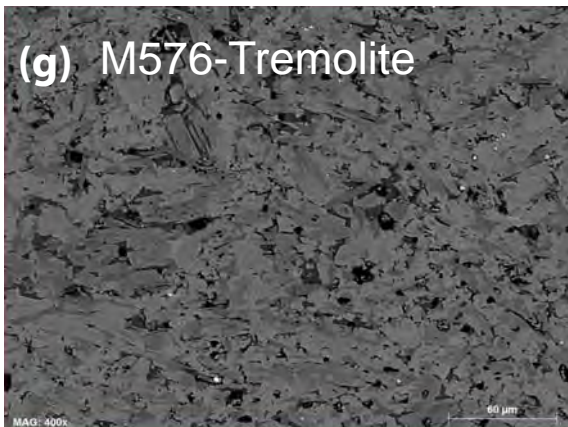
(e) M567-Hastingsite



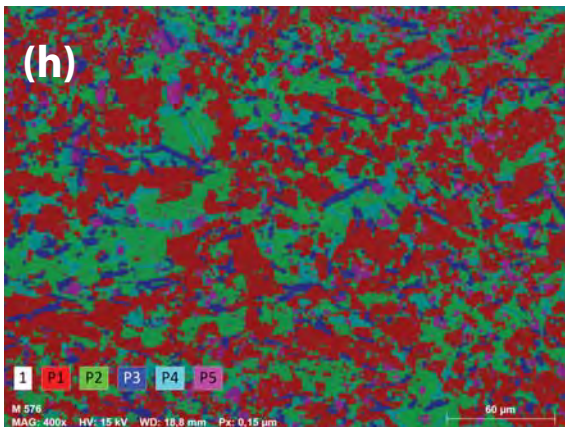
(f)

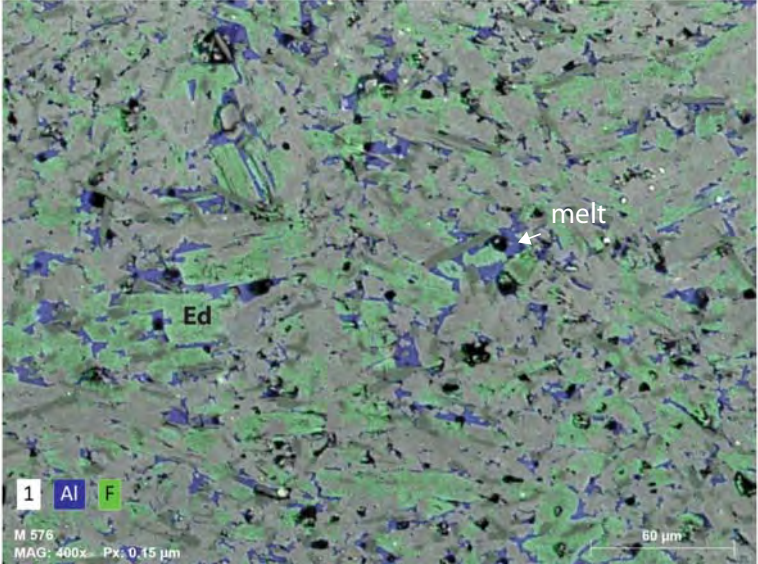


(g) M576-Tremolite



(h)





melt

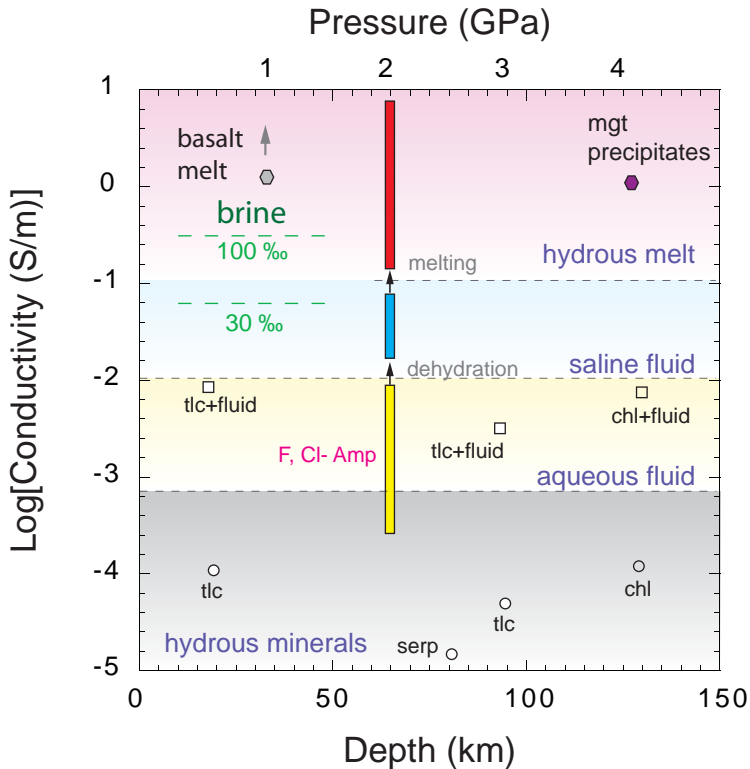


Ed

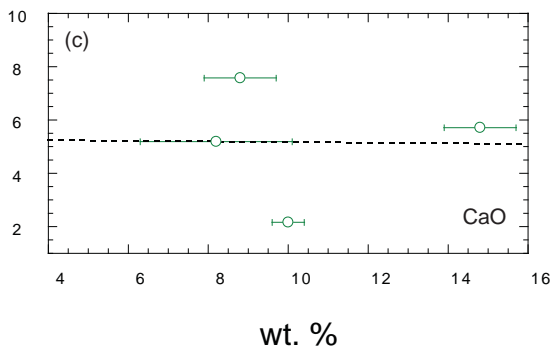
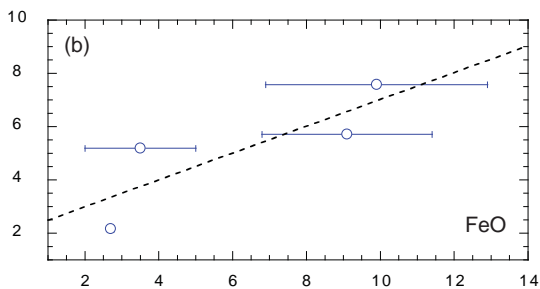
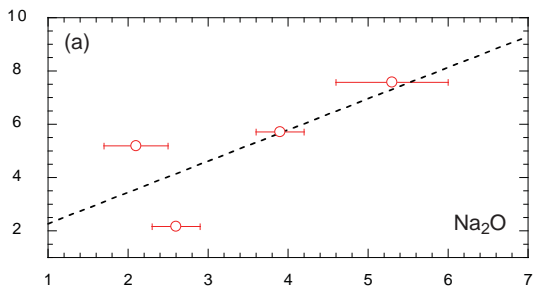
1 Al F

M 576
MAG: 400x Px: 0.15 μm

60 μm



Electrical conductivity of melt (S/m)



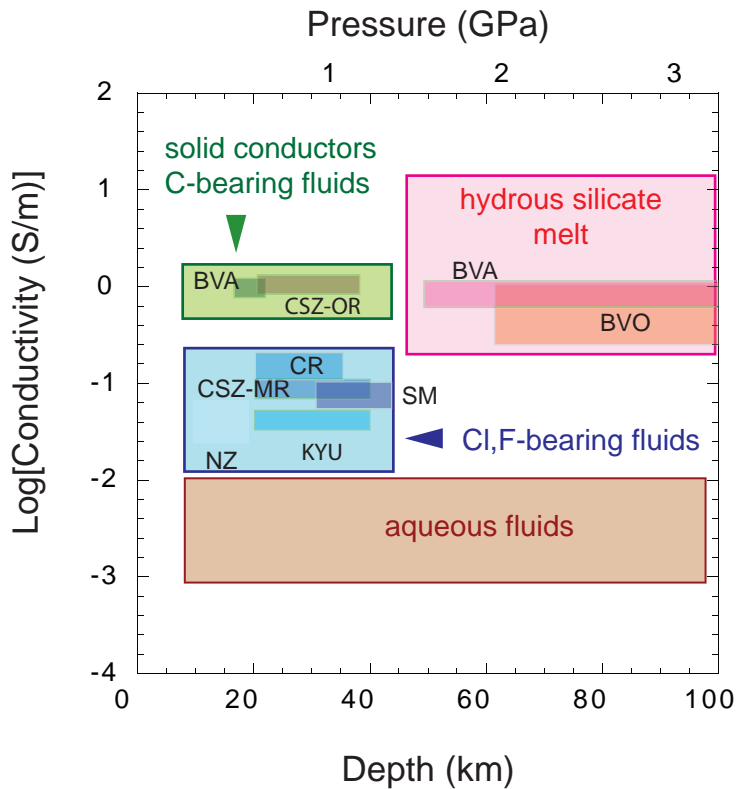


Table 1. Experimental conditions

Exp.	P (GPa)	T₁ (K)	T₂ (K)	Reaction	% rest
M554	1.5	933	1392	Fe Kaersutite = 0.50 Gt + 0.18 Ol + 0.32 Liq (melt)	62
M555	1.5	923	1258	Actinolite = 0.58 Cpx + 0.14 Opx + 0.28 Liq (melt)	0
M567	1.5	1091	1301	Hastingsite = 0.58 Kearsutite + 0.01 Opx + 0.42 Liq (melt)	76
M576	1.5	915	1402	Tremolite = 0.70 Cpx + 0.15 Opx + 0.17 Liq (Low T) Tremolite = 0.35 Edenite + 0.65 Liq (High T)	47

Exp., experiment run number. P, the pressure condition of the experiment. T₁ and T₂, temperature conditions corresponding to the interval of the reaction, identified on the bases of the activation enthalpy. Reaction, mineral assemblages are expressed as a product stoichiometry determined by mass-balance calculations with the procedure described in Wu and Koga (2013). Phase compositions are given in Table 2. The starting amphibole is taken as unity. % rest, the fraction of initial amphibole remained in the experiment at the end of the experiment, determined by SEM image analysis.

Table 2. Composition of mineral phases after dehydration and melting

Phase	Fe-Krs=Gt+Ol+liq				Act=Cpx+Opx+liq				Hst=Krs+En+Liq				Tr=F-Ed+liq		
	Krs*	Gt	Ol	Melt	Act*	Cpx	Opx	Melt	Hst*	Krs	En	Melt	Tr*	F-Ed	melt
SiO₂	39.0(7)	40.2(14)	34.9(17)	42.2(31)	57.1(8)	55.2(2)	57.1(5)	61.0(28)	43.1(13)	38.4(8)	58.9(2)	48.3(29)	56.9(8)	56.00(5)	55.2(4)
TiO₂	5.4(2)	7.6(2)	3.37(6)	3.5(7)	0.03(4)	0.04(1)	0.01(2)	0.03(14)	3.8(6)	5.1(5)	0.06(1)	2.2(17)	0.08(4)	0.17(3)	0.23(5)
Al₂O₃	13.9(3)	15.1(13)	7.4(9)	16.6(21)	1.18(9)	1.4(4)	0.9(4)	0.8(8)	9.7(7)	14.8(5)	0.31(3)	2.9(19)	1.3(1)	1.28(9)	1.7(2)
Cr₂O₃	0.02(2)	0.02(1)	0.00	0.02(7)	0.00	0.00	0.00	0.00	0.02(2)	0.04(3)	0.003(4)	0.00	0.00	0.00	0.00
FeO	11.2(5)	9.8(9)	20.4(19)	9.1(23)	4.9(4)	5.1(4)	7.3(3)	3.5(15)	13.7(12)	16.4(8)	3.84(2)	9.9(30)	2.9(3)	2.79(5)	2.6(1)
MnO	0.10(3)	0.11(0)	0.15(5)	0.08(9)	0.3(2)	0.40(3)	0.42(4)	0.00	0.23(9)	0.26(5)	0.06(1)	0.2(2)	0.1(1)	0.08(2)	0.07(3)
MgO	11.9(4)	12.3(9)	24.4(6)	5.4(19)	21.1(3)	21.1(7)	30.6(3)	16.3(19)	13.1(5)	8.5(5)	33.9(7)	18.5(14)	22.4(3)	24.6(9)	23.2(5)
CaO	11.6(2)	12.0(4)	6.3(8)	14.8(9)	11.6(2)	15.5(8)	2.5(4)	8.2(19)	9.9(4)	10.8(2)	2.7(1)	8.8(9)	12.7(2)	9.6(11)	10.0(4)
Na₂O	2.16(8)	1.6(1)	0.71(0)	3.9(3)	0.8(1)	0.28(7)	0.05(2)	2.1(4)	3.9(3)	2.9(2)	0.08(5)	5.3(7)	1.0(1)	1.94(9)	2.6(3)
K₂O	1.65(9)	1.9(1)	0.27(4)	2.1(4)	0.05(2)	0.01(1)	0.01(0)	0.17(9)	0.16(2)	0.16(2)	0.06(8)	0.16(7)	0.38(4)	0.75(4)	1.1(1)
F	0.17(2)	0.34(8)	0.00	0.00	0.02(0)	0.00	0.00	0.09(11)	0.21(8)	0.22(1)	0.48(10)	0.18(20)	0.79(2)	3.3(4)	0.1(1)
Cl	0.022(2)	0.03(1)	0.00	0.02(4)	0.004(1)	0.00	0.00	0.01(11)	0.03(3)	0.006(5)	1.02(5)	0.03(7)	0.012(2)	0.03(4)	0.01(1)
H₂O+	0.71(5)	0.00	0.00	2.3(3)	2.16(5)	0.00	0.00	7.7(2)	1.92(4)	0.72(21)	0.00	3.6(3)	1.63(4)	0.01(10)	2.56(5)
Total	97.87	101.01	97.61	100.00	99.24	99.01	98.82	100.00	99.88	98.41	101.48	100.00	100.18	100.58	99.17

Measurements by an electron microprobe are reported here. Values in parentheses represent one standard deviation on the averages in terms of the smallest units cited. For example, 39.0(7) should read as 39.0 +/- 0.7. H₂O+: the values are determined by the stoichiometric balance of amphibole composition following the procedure of Locock (2014). Met compositions are determined by a modified mass-balance procedure (Wu and Koga 2013). *starting amphiboles remaining in the sample after the dehydration-melting